

## Electronic Supplementary Information (ESI):

### Bubbles no more: In-plane trapping and removal of bubbles in microfluidic devices

Conrad Lochovsky, Sanjesh Yasotharan and Axel Günther

Supplementary Text, Supplementary Figures S1–S6,  
Supplementary Tables S7, Supplementary References

#### S1 Increase in wall shear stress due to presence of a bubble

In the following, we briefly estimate the amplification in wall shear stress that is attributed to a gas bubble passing through a liquid-filled microchannel with a rectangular cross section. We assume a channel width of  $w = 200 \mu\text{m}$  and a depth of  $h = 150 \mu\text{m}$ , corresponding to a hydraulic diameter  $d_h = 171 \mu\text{m}$ . We further consider an aqueous surfactant solution (viscosity  $\mu = 6.92 \times 10^{-4} \text{ Pa}\cdot\text{s}$ , interfacial tension  $\gamma \sim 0.025 \text{ N/m}$ , temperature  $37^\circ\text{C}$ ) that preferentially wets the walls and perfuses the microchannel at a volumetric flow rate  $Q = 10 \mu\text{L/min}$ . The wall shear stress in the absence of a bubble and for fully-developed laminar flow can be estimated as  $\tau_w = 32Q\mu\pi^{-1}d_h^{-3} = 0.23 \text{ Pa}$  ( $2.3 \text{ dyn/cm}^2$ ). If a long bubble is present, a liquid film of thickness  $\delta$  covers the four side walls. We assume the bubble to travel at a velocity similar to the superficial velocity of the liquid,  $U = QLw^{-1}h^{-1}$ , and obtain the capillary number,  $Ca = \mu U \gamma^{-1} = 1.5 \times 10^{-4}$ . Bretherton's equation<sup>1</sup> can be used. However note that for the considered small  $Ca$  the equation's estimate of the film thickness,  $0.67Ca^{2/3}d_h \sim 0.33 \mu\text{m}$ , is somewhat smaller than values reported by Schwartz *et al.* and Chen<sup>2</sup>. A larger film thickness is therefore expected, in part due to surface tension gradients (i.e., Marangoni effects). We therefore estimate the wall shear stress due to the presence of a bubble in a microchannel that is perfused with culture medium to be increased by a factor of  $\phi(Ca = 1.5 \times 10^{-4}) = \tau_{w,B} / \tau_w = 40\text{--}66$ , as compared to the bubble-free case. The upper limit,  $\phi = 1 / (5.35 \cdot Ca^{2/3}) = 66$ , is given by Bretherton's equation.

#### S2 Materials and methods

This section summarizes the fabrication procedures and detailed microfluidic device designs

##### Microfluidic device designs

The presented bubble trap design is compatible with single-layer soft lithography. The three employed device designs are shown in Figures S1–S3. While the bubble trap only requires a single layer, a second layer was introduced in all devices to allow bubble trapping and removal to be systematically investigated by controllably generating gas bubbles upstream of the trap location. Figure S1 shows the layout of the two-layer microfluidic device that was employed in an experimental setup to characterize single-trap behaviour, Fig. 2. The results shown in Figs. 3 and 4a were obtained using this device. Figure S2 shows the layout of a two-layer device with eight parallel traps that led to the results shown in Figs. 4b,c. Figure S3 shows the microchannel network for a

two-layer device that was used to demonstrate the consistent use of three bubble traps for on-chip studies of intact small blood vessels<sup>3</sup> (see also Fig. 4d). A resistance artery segment (length  $\sim 1 \text{ mm}$ , diameter  $\sim 250 \mu\text{m}$ ) was selectively perfused on the inside (lumen) and superfused on the outside. Bubble traps were located upstream of the blood vessels in the perfusing and superfusing streams.

Microfluidic channel networks were defined with a computer aided design program (AutoCAD, Autodesk Inc., San Rafael, CA, USA) and transferred to transparency masks at a spatial resolution of approximately  $10 \mu\text{m}$  (20,000 dpi, CAD/ART Services, Bandon, OR, USA). Masters were fabricated using standard photolithographic techniques.<sup>4</sup> Briefly, negative resist SU-8 25 (Microchem, Newton, MA, USA) was spun (2000 rpm, 30 s) onto a pre-cleaned and dehydrated glass slide ( $75 \text{ mm} \times 50 \text{ mm} \times 1 \text{ mm}$ , Thermo Fischer Scientific, Waltham, MA, USA) to form a  $25 \mu\text{m}$  thin initial layer that was subsequently pre-baked and flood-exposed under UV light. Two additional layers of SU-8 2050 were sequentially spun at 1,750 rpm and pre-baked. The combined SU-8 feature layer had a total height of  $150 \mu\text{m}$  and was UV exposed (wavelength:  $365 \text{ nm}$ , total energy:  $240 \text{ mJ/cm}^2$ , model 200 Mask Aligner, Optical Associates International Inc., San Jose, CA, USA) through a transparency mask, prior to a subsequent development step (SU-8 Developer, Microchem, Newton, MA, USA). The depth and uniformity of the feature layer was verified using an optical profilometer (Wyko NT1100, Veeco Instruments, Woodbury, NY, USA; see also ESI S2). PDMS (Sylgard 184 Elastomer Kit, Dow Corning Corp., Midland, MI, USA) was mixed at a 10:1 base-to-catalyst ratio and degassed both before and after pouring over the masters and subsequently cured at  $80^\circ\text{C}$  for 2 h. In the case of two-layer microfluidic devices that contained on-chip valves for on-demand bubble formation, a  $500 \mu\text{m}$  thick layer of PDMS was spincoated at 450 rpm for 30 s to form the bottom fluidic layer resulting in a  $350 \mu\text{m}$  thick membrane between the two fluidic layers. The separate layers were first partially cured at  $80^\circ\text{C}$  for approximately 15 min on their respective masters. The upper control layer was then peeled from its master before aligning and manually compressing it onto the bottom fluidic layer. The two-layer substrate was cured overnight, peeled from the second master and cut to a footprint of either  $75 \text{ mm} \times 50 \text{ mm}$  (device shown in Fig. S2) or  $75 \text{ mm} \times 25 \text{ mm}$  (devices shown in Figs. S1,S2). After  $0.8 \text{ mm}$  diameter holes were manually punched, the PDMS substrate was surface treated in an oxygen plasma (model PDC-001, Harrick Plasma, Ithaca, NY, USA) for 30 s and bonded to a  $1 \text{ mm}$  thick glass slide (VWR, West Chester, PA, USA). To define the on-chip valves, glass slides were spincoated with CYTOP, an amorphous fluoropolymer (CTL-809-A, Bellex International Corp., Wilmington, DE, USA) at 600 rpm for 22 s, prior to plasma treatment. CYTOP patterns

## Electronic Supplementary Information (ESI): Bubbles no more: In-plane trapping and removal of bubbles in microfluidic devices Conrad Lochovsky, Sanjesh Yasotharan and Axel Günther

were transferred via microcontact printing using a PDMS stamp to the valve region on the two-layer substrate, to locally prevent bonding to the glass slide in those regions. Passivated stainless steel pins (length: 12.7 mm, size: 23 gauge, New England Small Tube Corp., Litchfield, NH, USA) were inserted in the holes of the microfluidic device, secured using epoxy, and connected to Tygon tubing (0.02"ID, 0.06"OD, Cole-Parmer, Vernon Hills, IL, USA) which provided the fluidic connections (Upchurch Scientific, Oak Harbor, WA, USA) to syringes, vacuum pumps, and 20 mL glass vials.

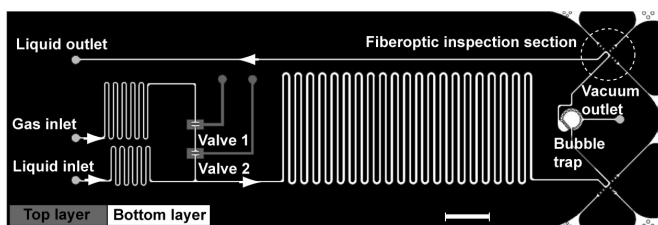


**Figure S1:** Two-layer microfluidic chip design for the controlled formation of gas bubbles. Liquid is passing through the microchannel network in the bottom layer (indicated in white colour) where single bubbles are controllably injected and subsequently removed using a bubble trap. The second pneumatic (control) layer is indicated in gray colour. Scale bar is 5 mm.

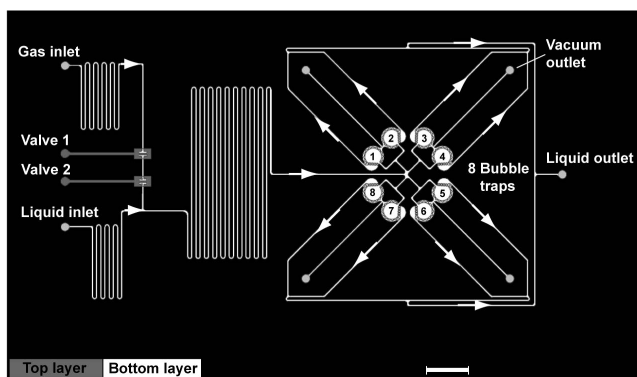


**Figure S2:** Two-layer microfluidic chip design for a configuration consisting of eight parallel traps. Liquid is passing through the microchannel network in the bottom layer (indicated in white colour) where single bubbles are controllably injected and subsequently removed. The second pneumatic (control) layer is indicated in gray colour. Scale bar is 5 mm.

The depth and uniformity of channel features in the SU8 masters was determined using an optical profilometer. Measurements were performed at multiple points within a region of interest (ROI) that included the bubble trap, typically at four points along the circumference of the trapping chamber, and at locations away from the ROI. The average channel height within the ROI typically showed a feature depth variation of smaller than 1  $\mu\text{m}$  for each inspected master.

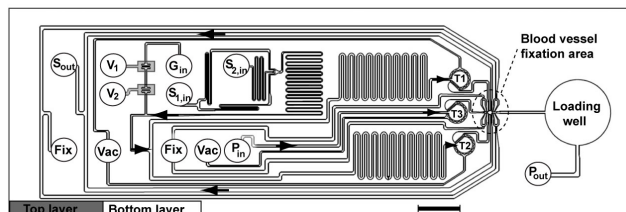


**Figure S3:** Layout of two-layer microfluidic chip for the on chip investigation of mouse mesenteric artery segments<sup>3</sup>. The pneumatic control layer is indicated in gray colour. Symbols  $S_{1,in}$  and  $S_{2,in}$  indicate the superfusion inlets,  $P_{in}$  is the superfusion inlet,  $S_{out}$  the superfusion outlet and  $P_{out}$  the perfusion outlet.  $G_{in}$  is the inlet for the gas,  $Vac$  is the vacuum outlet and  $Fix$  denotes the outlets located downstream of the small blood vessel fixation channels.  $V_1$  and  $V_2$  indicate the control inlets for two on-chip valves. Scale bar is 5 mm.

Detailed design files of the bubble traps are available from the authors upon request or download from their research group website (<http://mfl.mie.utoronto.ca/>).

### Experimental setup

Liquid flow rates were established using syringe pumps (PHD 2000, Harvard Apparatus, Holliston, MA, USA). A syringe was primed with one of the following working liquids: de-ionized and filtered water, ethanol, or an aqueous solution containing 0.01M poly(ethylene-glycol) (20)sorbitan monolaurate (Tween 20, Sigma Aldrich, St. Louis, MO, USA), 1% wt bovine serum albumin (BSA, Sigma Alrich), or the biological buffer 3-(N-morpholino) propanesulfonic acid (MOPS) (see ESI Table S1.3) and connected to the liquid inlet of the device. A compressed gas cylinder either containing purified  $N_2$  (99.998%) or purified  $CO_2$  (99.8%) (Linde Canada Ltd., Mississauga, ON, Canada), was connected via a combination pressure regulator (full scale 15 psi, Condyne P/N: PR50A15Z1, Valco Instruments Comp. Inc., Houston, TX, USA) to the gas inlet on the device. Gas bubbles were controllably added to the liquid stream at a T-junction on-demand, by operating two normally-closed on-chip valves. The valves were actuated by a miniature pump (CTS series, Hargraves Technology Corp., Mooresville, NC, USA) that selectively applied a vacuum or an overpressure. Separate miniature pneumatic valves (model LHLA-05-2111H, Lee Comp., Westbrook, CT, USA) were connected to a manifold (model LFAA three-valve manifold) and controlled via a custom Labview software program (Labview version DS1, National Instruments, Austin, TX, USA) and a 14-bit USB data acquisition interface (USB-6009, National Instruments), which selected between the two pressure levels and thereby switched between the valve "open" or the "closed" positions. The vacuum necessary to operate the bubble traps was supplied using either a miniature vacuum pump (CTS series,

## Electronic Supplementary Information (ESI):

### Bubbles no more: In-plane trapping and removal of bubbles in microfluidic devices

Conrad Lochovsky, Sanjesh Yasotharan and Axel Günther

Hargraves Technology Corp.; differential pressures: 40.6 kPa or 74.5 kPa,) or a direct drive vacuum pump (model#: 8917A, Gardner Denver Welch Vacuum Technology Corp., Niles, IL, USA; differential pressure: 96.5 kPa). Pressure measurements were manually taken from a vacuum gauge and recorded with a piezoresistive transducer (140PC series, Honeywell, Morristown, NJ, USA). Poly(vinyl chloride) (PVC) tubing (total length approximately 30 cm, 1/8" ID, VWR, West Chester, PA, USA) was used to connect the vacuum pump with the microfluidic device via fittings (McMaster-Carr, Elmhurst, IL, USA). Separate devices were used to determine the gas removal rates for the different working fluids in order to prevent any surface or material cross-contamination. At least two different devices were used for measurements at each condition.

#### Numerical simulations

Numerical simulations were carried out using the software program Comsol (Comsol, Inc., Burlington, MA, USA). Numerical grids with approximately 75,000 elements were generated. Solutions were obtained sequentially for stationary conditions using a direct linear solver (Umfpack) with a relative tolerance of  $1 \times 10^{-6}$ . We numerically model the removal of a trapped  $N_2$  bubble of a fixed size and shape that is surrounded by water through the inter-channel wall into the vacuum channel. A temperature of 298K and ambient pressure (1 atm) were assumed for the steady state simulation. For the inflowing liquid and at the gas-liquid interfaces, the dissolved  $N_2$  concentration corresponded to the saturation value,  $0.61 \text{ mol/m}^3$ . Concentrations at the PDMS- $N_2$  and PDMS-vacuum boundaries were determined from solubility data of  $N_2$  in PDMS to be  $3.87 \text{ mol/m}^3$  and  $1.02 \text{ mol/m}^3$ , respectively. We consider  $N_2$  to be a low-sorbing penetrant, i.e. its solubility in the PDMS substrate is independent of pressure and its concentration is proportional to pressure. The stiff spring method was employed to maintain continuity of the mass flow in the numerical solution. The diffusivity of  $N_2$  in  $H_2O$  is  $1.88 \times 10^{-9} \text{ m}^2 \text{ s}^{-1}$  (298K).<sup>5</sup> With a relationship given by Merkel *et al.* (Eqn. 23),<sup>6</sup> we determined the diffusivity of  $N_2$  in PDMS at  $T = 298\text{K}$  and  $\Delta p = 96.5 \text{ kPa}$  to be  $3.39 \times 10^{-9} \text{ m}^2 \text{ s}^{-1}$ , a value similar to literature data.<sup>7</sup> The positions of the  $N_2$ - $H_2O$  and  $N_2$ -PDMS interfaces were extracted from bright-field images. As long as a bubble was not large enough to block the entire trapping area, the liquid flow through the trap was not markedly affected due to the low Reynolds number of the flow (see Fig. S4a).

For  $Q = 16.7 \mu\text{L}/\text{min}$ , Fig. S4a shows the dissolved  $N_2$  concentration in the PDMS and  $H_2O$  in proximity of a trapped bubble. Figure S4b compares experimentally and numerically obtained bubble removal rates. Experimental data represented a time-average of the gas removal rate over 30 s. The simulation was carried out for a bubble shape that

corresponded to centre of this time interval, i.e. the 15 s point.

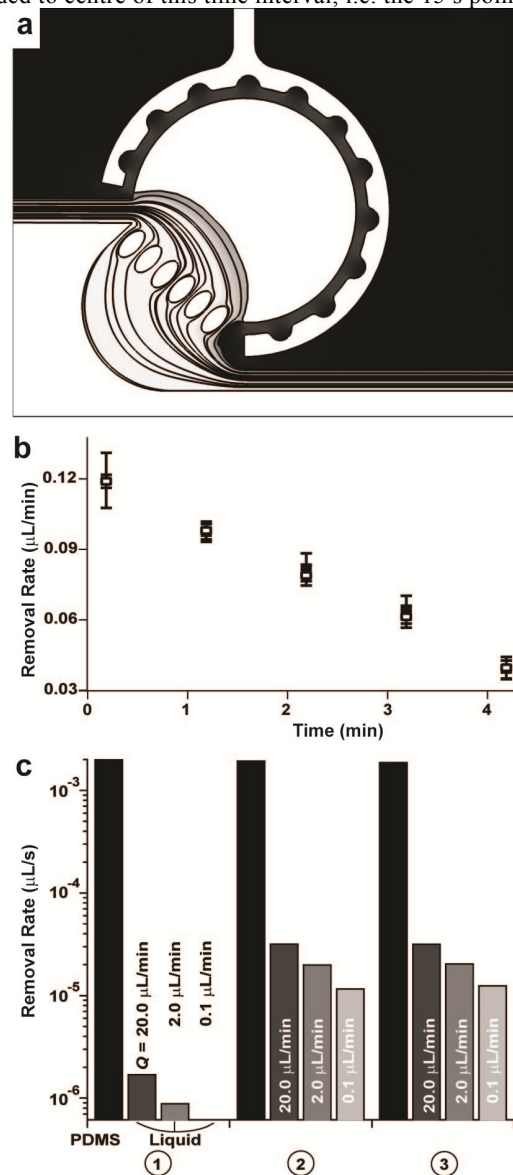


**Figure S4:** (a) Dissolved gas concentration and fluid velocity obtained from a numerical model of mass transfer from a trapped bubble across the interchannel wall and into the perfusing liquid stream. The liquid was assumed saturated at the inflow section with  $Q = 16.7 \mu\text{L}/\text{min}$ . Streamlines indicate the velocity field; contours denote the concentration in liquid phase. (b) Numerically predicted removal rate ( $\square$ ) compared with experimental results ( $\blacksquare$ ) for bubbles removed at  $Q = 20 \mu\text{L}/\text{min}$ ,  $\Delta p = 96.5 \text{ kPa}$  ( $n=5$ ). (c) The majority of the gas was removed via permeation from the bubble directly through the PDMS substrate (black) with the remainder ( $\leq 2\%$ ) being transported through the liquid (gray shades corresponding to  $Q = 0.1, 2$  and  $20 \mu\text{L}/\text{min}$ ).

The experimental and numerical results were obtained for  $Q = 20 \mu\text{L}/\text{min}$ ,  $\Delta p = 96.5 \text{ kPa}$ . Removal rates were obtained for  $n = 5$  bubbles of similar size and morphology. Error bars

## Electronic Supplementary Information (ESI):

### Bubbles no more: In-plane trapping and removal of bubbles in microfluidic devices

Conrad Lochovsky, Sanjesh Yasotharan and Axel Günther

represent  $\pm 1$  standard deviation for both the experimental and numerical results. Good agreement was found between experimentally obtained and numerically predicted removal rates. At  $Q = 20 \mu\text{L}/\text{min}$ , numerical simulations indicated the majority of gas removal taking place through the PDMS-gas interface with  $< 2\%$  of the total flux being transported through the bubble-liquid interface (Fig. S4c). The convective influence of liquid flow on gas transport from a trapped bubble was also investigated at reduced perfusion rates  $Q = 0.1 \mu\text{L}/\text{min}$  and  $2 \mu\text{L}/\text{min}$  shown to be small in comparison to the flux through the PDMS surface.

Note the effect of the continuously operated bubble trap on decreasing the dissolved gas concentration in the perfusing liquid stream, whether or not a bubble is present in the trap.

## S3 Results

### Permeation

In addition to geometrical parameters, the achievable removal rate is dependent on the permeability of the considered gas in PDMS. Permeabilities of the relevant gasses  $\text{CO}_2$ ,  $\text{O}_2$  and  $\text{N}_2$  in PDMS are tabulated in the literature<sup>8,9</sup> and summarized in Table S7. Literature data show significant variability that may be attributed to the experimental setup, temperature influences and to some extent also in the variability in the used PDMS chemistry. We designed and fabricated a dedicated microfluidic device with a  $150 \mu\text{m}$  deep microchannel network to assess the permeability of the PDMS kit most commonly used in microfluidic device fabrication, Sylgard 184 Elastomer Kit (Dow Corning, Midland, MI, USA). The device consists of a microchannel with a length exceeding  $50 \text{ cm}$ . At the downstream end, a vacuum channel lined the flow channel over a distance of  $\lambda = 10 \text{ cm}$  and was separated by a  $b = 200 \mu\text{m}$  wide inter-channel wall (Fig. S4a). Equally sized gas bubbles were obtained via passive breakup in a segmented flow in a meandering channel section that was located upstream of the location where the permeation measurement was obtained. After the perfusion flow was stopped, a defined pressure difference  $\Delta p$  was applied across the interchannel wall. A time-series of bright-field micrographs of bubbles was obtained in a field of view that included the inter-channel wall (see Fig. S4a, inset) and allowed the rate of gas removal to be determined.

Figure S4b shows a cross-section of the bubble-containing channel and the neighbouring vacuum channel. As indicated by the arrows, permeation occurs not only in-plane, i.e., through the area  $A = \Lambda_B h$  of the interchannel side wall, but has an out-of-plane component through the top wall of the channel as well. The bottom glass wall is gas impermeable. To quantitatively assess the in-plane and out-of-plane contributions, we numerically estimated the permeation of  $\text{N}_2$  in a two-dimensional domain (temperature of  $298\text{K}$ ,

diffusivity of  $3.39 \times 10^{-9} \text{ m}^2 \text{ s}^{-1}$ ). Figure S4b shows the spatial distribution of the  $\text{N}_2$  concentration in the device cross section. The  $\text{N}_2$  concentrations of  $3.87 \text{ mol}/\text{m}^3$  and  $1.02 \text{ mol}/\text{m}^3$  were used as boundary conditions at the PDMS -  $\text{N}_2$  and the PDMS - vacuum interfaces, corresponding to the gas solubilities at atmospheric pressure and at  $\Delta p = 74.5 \text{ kPa}$ , respectively. Since the sharp corners of the PDMS channel's rectangular cross section introduced numerical challenges, small finite curvature radii ( $r = 50 \mu\text{m}$ ,  $10 \mu\text{m}$ ) were initially considered to determine the asymptotic value  $\xi(r \rightarrow 0) = J_{total} / J_{in-plane} = 1.23$ .

We consider a gas bubble with an average length  $\Lambda_B$  and a static contact angle of approximately  $90^\circ$ , based on experimental data and from literature indicating contact angles of approximately  $100^\circ$ .<sup>10</sup> We therefore assume the gas-liquid interfaces at the front and the end of a bubble to be flat and the side walls not to be covered by a liquid film. The permeability can be expressed in terms of the gas removal rate as

$$P = b[\xi A(p - p_0)]^{-1} dV_B / dt \quad (1)$$

where  $\xi$  takes into account in-plane and out-of-plane transport,  $P$  is the gas permeability in the PDMS substrate,  $A$  is the area of the side wall and  $\Delta p = (p - p_0)$  is the pressure difference applied across the interchannel wall. For a given channel geometry ( $w_L$ ,  $w_v$ ,  $b$ ,  $H$ ), Eqn. (1) can be used to determine  $P$  from measured values of  $dV_B/dt$ . Figure 2c shows the obtained results along with literature data (see also Table S7).<sup>6, 11-18</sup>

Figure S5 shows the detailed layout of the microfluidic device used for the results reported in Fig. S4.

We numerically estimated the effect of the selected side wall geometry on the measured gas removal rate, Fig. S6. An approximately 13% faster removal rate was estimated for three different  $\text{N}_2$  bubbles that were trapped in de-ionized and filtered water when an interchannel wall of uniform thickness  $b = 100 \mu\text{m}$  was considered instead of the experimentally employed geometry (Fig. 1c) that was selected in favor of an increased fabrication yield.

Electronic Supplementary Information (ESI):

Bubbles no more: In-plane trapping and removal of bubbles in microfluidic devices

Conrad Lochovsky, Sanjesh Yasotharan and Axel Günther

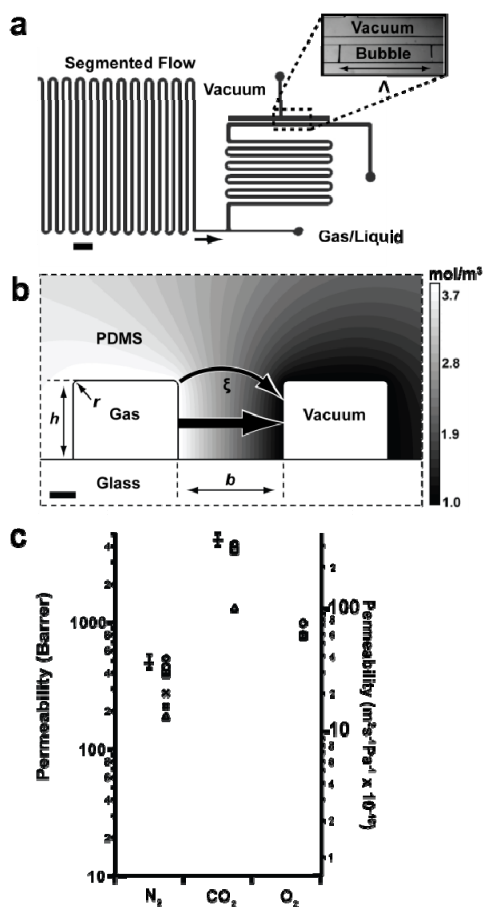


**Figure S4** (a) Schematic of single-layer PDMS device to assess the permeability of pure gasses. Inset shows bright-field micrograph of bubble in a liquid-filled channel being removed by gas permeation into vacuum channel. Scale bar is 1 mm. (b) Device cross-section including channel filled with gas bubble, gas-permeable PDMS substrate including inter-channel wall (width  $b$ , height  $h$ ) and top channel wall, and impermeable glass bottom wall. Numerically predicted dissolved  $N_2$  concentrations in the substrate. Arrows indicate in-plane and out-of-plane contributions to transport. (c) Literature ( $\Delta$ <sup>18</sup>,  $\square$ <sup>6</sup>,  $\circ$ <sup>17</sup>,  $\diamond$ <sup>13</sup>,  $*$ <sup>19</sup>,  $\#$ <sup>11</sup>,  $\times$ <sup>14</sup>,  $+$ <sup>12</sup>, see also Table S7) and present measurement data (error bars indicate standard deviations, out-of-plane transport was taken into account by using  $\xi = 1.23$ ) for the permeability of  $N_2$  and  $CO_2$  in PDMS.

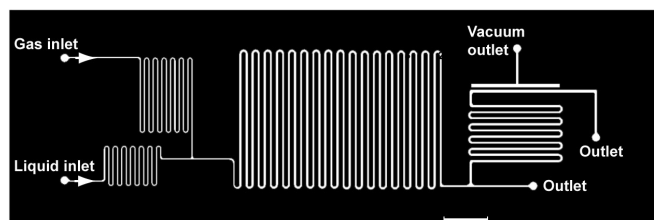


**Figure S5:** Single-layer microfluidic chip design used for permeability measurements. The PDMS substrate and microchannel network are represented in black and white colours, respectively. Scale bar is 5mm.

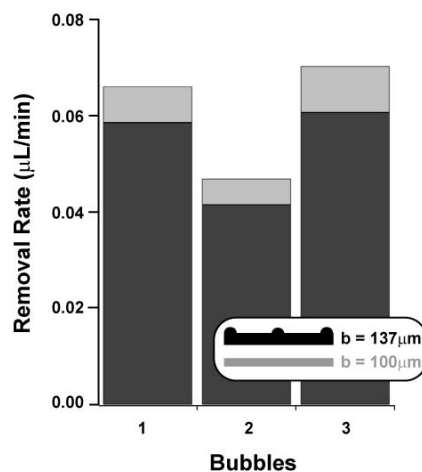


**Figure S6:** Simulated removal rate for two different configurations of the interchannel wall in the otherwise identical bubble trap design (Fig. 2a,b). Gray colour indicates a uniform thickness  $b = 100 \mu\text{m}$  (gray), black colour indicates the experimentally considered case with equidistant support elements,  $b = 137 \mu\text{m}$ .

**Table S7** Literature permeability and diffusivity data for pure gasses in poly-(dimethylsiloxane). Temperatures are listed in brackets.

Gas	Permeability (1 Barrer = $10^{-10} (\text{cm}^3 \text{O}_2) \text{ cm cm}^{-2} \text{ s}^{-1} \text{ cmHg}^{-1}$ $= 7.5 \times 10^{-18} \text{ m}^2 \text{ Pa}^{-1} \text{ s}^{-1}$ )	Diffusivity ( $\text{cm}^2/\text{s}$ )
$N_2$	245 (20C) <sup>16</sup> , 280 (20C) <sup>14</sup> , 256 (25C), 395 (25C) <sup>12</sup> , 180 $\pm$ 20 (28C) <sup>18</sup> , 400 $\pm$ 10 (35C) <sup>6</sup> , 450 (35C) <sup>17</sup> , 525 (35C) <sup>13</sup> , 220 (40C) <sup>11</sup>	130 $\pm$ 4 (28C) <sup>18</sup> , 34 $\pm$ 1 (35C) <sup>6</sup>
$O_2$	825 (25C) <sup>12</sup> , 800 $\pm$ 20 (28C) <sup>6</sup> , 1000 (35C) <sup>17</sup>	34 $\pm$ 1 (35C) <sup>6</sup>
$CO_2$	1300 $\pm$ 200 (28C) <sup>18</sup> , 3800 $\pm$ 70 (35C) <sup>6</sup> , 4200 (35C) <sup>17</sup> , 5600 (35C) <sup>13</sup>	110 $\pm$ 10 (28C) <sup>18</sup> , 22 $\pm$ 1 (35C) <sup>6</sup>

## Electronic Supplementary Information (ESI):

### Bubbles no more: In-plane trapping and removal of bubbles in microfluidic devices

Conrad Lochovsky, Sanjesh Yasotharan and Axel Günther

#### Supplementary references

1. F. Bretherton, *Journal of Fluid Mechanics*, 1961, **10**, 166-188.
2. J. Ratulowski and H. C. Chang, *Journal of Fluid Mechanics*, 1990, **210**, 303-328.
3. A. Günther, S. Yasotharan, A. Vagaon, C. Lochovsky, C. Lau, J. Voigtlaender-Bolz and S. Bolz, *Lab on a Chip*, 2010, **10**, 2341.
4. Y. Xia and G. Whitesides, *Annual Review of Materials Science*, 1998, **28**, 153-184.
5. E. Cussler, *Diffusion*, Cambridge University Press, Cambridge, 1984.
6. T. Merkel, V. Bondar, K. Nagai, B. Freeman and Y. Yampolskii, *Journal of Polymer Science Part B: Polymer Physics*, 2000, **38**, 415-434.
7. S. Stern, *Journal of Membrane Science*, 1994, **94**, 1-65.
8. J. Kang, Y. Kim and J. Park, *Lab on a Chip*, 2008, **8**, 176-178.
9. A. Skelley and J. Voldman, *Lab on a Chip*, 2008, **8**, 1733-1737.
10. E. Ostuni, C. Chen, D. Ingber and G. Whitesides, *Langmuir*, 2001, **17**, 2828-2834.
11. R. W. Baker, N. Yoshioka, J. M. Mohr and A. J. Khan, *Journal of Membrane Science*, 1987, **31**, 259-271.
12. M. B. Hagg, *Journal of Membrane Science*, 2000, **170**, 173-190.
13. S. M. Jordan and W. J. Koros, *Journal of Polymer Science Part B-Polymer Physics*, 1990, **28**, 795-809.
14. M. Leeman, G. Eigenberger and H. Strathmann, *Journal of Membrane Science*, 1995, **113**, 313-322.
15. T. C. Merkel, R. P. Gupta, B. S. Turk and B. D. Freeman, *Journal of Membrane Science*, 2001, **191**, 85-94.
16. A. Singh, B. D. Freeman and I. Pinnau, *Journal of Polymer Science Part B-Polymer Physics*, 1998, **36**, 289-301.
17. S. A. Stern, V. M. Shah and B. J. Hardy, *Journal of Polymer Science Part B-Polymer Physics*, 1987, **25**, 1263-1298.
18. P. Tremblay, M. Savard, J. Vermette and R. Paquin, *Journal of Membrane Science*, 2006, **282**, 245-256.
19. W. Robb, *Ann. N. Y. Acad. Sci.*, 1968, **146**, 119.